


ORIGINAL ARTICLE

Open Access



Simulating Tensile and Compressive Failure Process of Concrete with a User-defined Bonded-Particle Model

Jinhui Ren , Zhenghong Tian* and Jingwu Bu

Abstract

A user-defined bonded-particle model (UBM) which is based on the modified parallel bond was established in this paper to investigate the tensile and compressive failure mechanism of concrete on the three-dimensional (3D) level. The contact constitutive relation and the failure criterion of the UBM can be added to the commercial discrete element software PFC^{3D} by compiling them as a dynamic link library file and loading it into PFC^{3D} whenever needed. In addition, the aggregate particles can be generated according to the volume fraction and the shape of each aggregate is irregular. Then, by comparing the results of numerical simulation with the results of laboratory tests, it is found that this bonded-particle model can simulate the tensile and compressive failure process of concrete well to a certain extent. Specifically, the two have basically similar failure patterns and stress–strain responses no matter under tension or compression loading condition. All results indicate that this UBM is a promising tool in understanding and predicting the tensile and compressive failure process of concrete.

Keywords: three-dimensional simulation, failure process, concrete, user-defined bonded-particle model, PFC^{3D}

1 Background

Concrete has been widely used as an extremely important building material for more than one century. During this period, a large number of scholars have made lots of in-depth research on its mechanical properties and failure mechanism. However, in most of the previous engineering application, people usually still treat concrete as a homogenous material and the macroscopic elastic–plastic theory is used to describe its whole process of deformation and failure in order to facilitate the study. Actually, the mechanical behaviors of concrete at macro-level are strongly affected by its mesoscopic structures (Nitka and Tejchman 2015), thus those simplifications of concrete are unreasonable from this perspective.

With the rapid development of the discrete element methods (DEM), a growing number of scholars come to use this approach in the field of granular materials (Baleviius et al. 2006; Kaianauskas et al. 2010; Latham

et al. 2013) and geotechnical engineering (Azevedo and Lemos 2013; Sarfarazi et al. 2014; Sarfarazi and Haeri 2016). The main advantage of DEM is the feasibility to model highly complex poly-dispersed systems by using the basic data on individual particles without making oversimplifying assumptions (Kaianauskas et al. 2010). So more and more researchers are striving to apply this approach to the simulation of concrete although some conventional methods, such as the finite difference, finite element and boundary element methods, can also simulate the concrete or concrete-like materials to some extent (You et al. 2012; Zhang et al. 2014; Shuguang and Qingbin 2015; Haeri et al. 2013; Haeri 2015). However, there are a significant portion of concrete models built on the two-dimensional (2D) level (Camborde et al. 2000; Brara et al. 2001; Nagai 2004; Wang 2008; Azevedo 2008; Azevedo et al. 2010; Kim and Buttlar 2009; Kim et al. 2009; Lian et al. 2011a, b; Haeri and Sarfarazi 2016) which are considered to be difficult to accurately capture the interlock effect of particles in the 3D domain (Chen et al. 2011). In addition, material responses of the 3D simulation become more ductile

*Correspondence: zhtianhhu@163.com

College of Water Conservancy and Hydropower Engineering, Hohai University, Nanjing 210098, China

Journal information: ISSN 1976-0485 / eISSN 2234-1315

compared with the results of 2D simulation and the stress fluctuations are relatively smaller due to a higher coordination number (Nitka and Tejchman 2015). Recently, 3D asphalt concrete simulation systems based on the Burger's model (Chen et al. 2011; Liu et al. 2012) and 3D fresh concrete simulation systems based on the Bingham model (Shyshko and Mechtcherine 2013; Remond and Pizette 2014; Mechtcherine and Shyshko 2015) or the linear-spring dashpot model (Tan et al. 2015) have been gradually built up. But due to the lack of relatively appropriate constitutive models, the 3D simulation achievements for ordinary concrete are still very few. Hentz et al. (2004) developed a 3D discrete element model to study the dynamic behavior of concrete at high strain rates and Nagai et al. (2005) also successfully put forward a 3D rigid body-spring model (RBSM) to predict the failure behavior of concrete. But it is a pity that the shape of the coarse aggregates in their models is spherical and that means the shape effects of aggregates are not discussed. Subsequently, Kozicki et al. described a quasi-static mechanism of fracture in concrete specimens under multiple loading conditions by using a 3D novel lattice model (Kozicki and Tejchman 2008; Kozicki and Donz 2008). Although the results are satisfactory, yet it is not found in their articles whether the model can also effectively simulate the concrete subject to compression. Recently, Nitka and Tejchman (2015) have attempted to reproduce the mechanical behaviors of concrete by using a 3D discrete element model YADE which was first developed in University of Grenoble. But for the sake of simplicity, the spheres were assumed to approximately simulate both the aggregates and mortar.

The intention of this paper is to present a 3D UBM of concrete which takes both the geometrical shapes and volume fraction of aggregates into consideration simultaneously. It is worth mentioning that this new model is able to unify the two loading conditions, namely tension and compression. In other words, it can simulate the mechanical behaviors of concrete well to a certain extent in two cases (tension and compression) by using the same UBM and the same set of model parameters. The rest of the paper is organized as follows: In Sect. 2, the 3D mathematical model of concrete specimen are presented in detail. Section 3 first explains the contact constitutive relation and the failure criterion of the UBM, then solves the problem how to assign the mesoscopic mechanical parameters to the model. Subsequently, a few contrast tests for numerical models and physical models are introduced in Sect. 4. Finally, the predicted results of the numerical simulation are compared with laboratory experimental measurements in Sect. 5, while the discussion and concluding remarks are given in Sect. 6.

2 3D Mathematical Model of Concrete Specimen

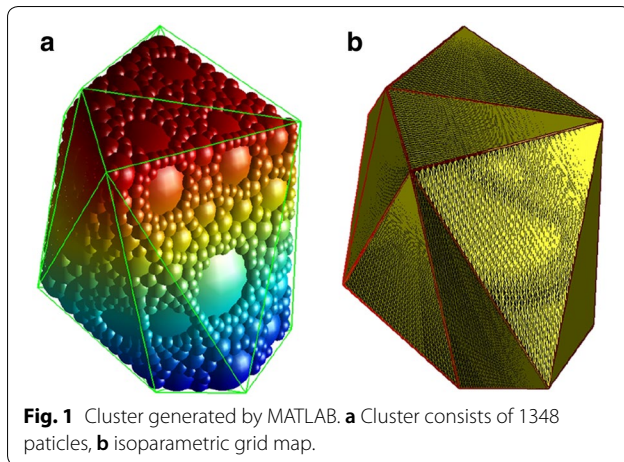
2.1 Generation and Replacement of Irregular Aggregate Particles

As a kind of heterogeneous material, concrete is usually assumed to be a three-phase composite consisting of aggregates, mortar and the interfacial transition zones (ITZs) between them. Scanning electron and backscattered electron micrography evidenced the zones of deficient clinker concentration to be 15–30 μm (Lian et al. 2011b). Here we use the average value of this range (namely 23 μm) as the thickness of ITZs. Its mechanical properties are influenced by the aggregate shapes to a certain extent. Piotrowska et al. (2014) pointed out the influence of coarse aggregate types on concrete behavior under high triaxial compression loading condition and Shigang et al. (2013) confirmed that the aggregate geometrical shapes has great effect on the failure behavior of the polyurethane polymer concrete (PPC) under tension. Rocco and Elices (2009) also explored the influence of aggregate shapes on the fracture energy, tensile strength and elastic modulus in concrete. What's more, according to the research of Azevedo and Lemos (2006), it is shown that non-circular particles will lead to an increase in the post-peak ductility both in tension and in compression when the heterogeneous approach is adopted. Thus it is especially necessary to generate irregular aggregate particles which can be regarded as polyhedrons if we want to simulate and predict the mechanical behaviors of concrete more precisely.

On account of the difficulty existing in the discrete element calculation with polyhedrons, the most convenient way of simulating polyhedrons is to bond the sphere particles into clumps. This idea can be achieved in PFC^{3D} by executing the relevant commands of clump. There are two points worth highlighting:

- The polyhedrons in this paper are all convex polyhedrons for the sake of simplicity.
- A clump itself will not break apart since it acts as a rigid body (with deformable boundaries).

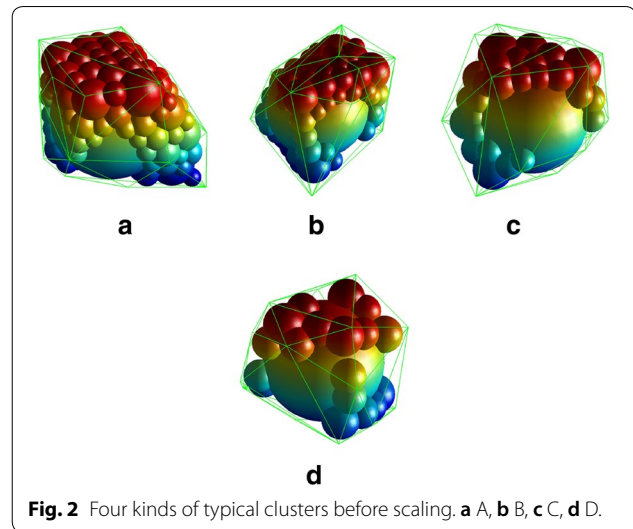
Before executing the commands of clump, we need to get some irregular particle clusters in advance and this process is implemented in the commercial software MATLAB. Theoretically, the smaller the particle sizes of clump internal structure spheres are and the larger the maximum allowable overlap is, the better the effect of finally generated polyhedron will be. For instance, a cluster consists of 1348 particles whose surface texture depth is only 0.142 mm and its isoparametric grid map used to calculate the surface texture depth generated by MATLAB are shown in Fig. 1a, b respectively. Then these clusters can be imported into PFC^{3D} to replace the sphere particles in corresponding



positions. We might as well call those sphere particles “locators” and their role is to provide specific location information and necessary space for the replacement of clusters. It should be emphasized that the “locators” are randomly generated according to the transformed volume fraction of aggregates and their diameters are specified as uniform distribution in corresponding gradation ranges. Therefore, prior to the replacement of a cluster, we need to perform equal proportional scaling operation to guarantee that its particle size is exactly equal to the diameter of the “locator” which remain to be replaced. Owing to the limited categories and fixed angles of the particle clusters generated in MATLAB, it certainly doesn’t conform the stochastic characteristics of aggregate distribution if the rotation operation is not carried out. For this reason, an algorithm for rotation developed by Dong et al. is adopted in this study (Dong et al. 2007). In order to give consideration to both the precision of aggregate shape and the efficiency of PFC^{3D} solver simultaneously, the aggregate models used in numerical tests can’t be as elaborate as that in Fig. 1a. At the same time, in order to reflect the difference of aggregate shape, this paper uses four kinds of typical particle clusters before scaling, which correspond to four kinds of size intervals in aggregate gradation respectively. Figure 2 displays the A, B, C and D four kinds of typical particle clusters before scaling which are adopted in numerical models and their detailed shape parameters are shown in Table 1. Descriptions for some of those shape parameters (coefficient of irregularity, angularity and surface texture depth) can be found in the relevant literature (Barrett 1980; Hentschel and Neil 2003; Pourghahramani and Forsberg 2005).

2.2 Generation of Full-Graded Concrete Cylinder Specimen Models

The diameter of concrete cylinder specimens is 72.0 mm and the height is about 156.0 mm. The reasons why its height is an approximate value are as follows:



- It is quite difficult to get an accurate model size since there is no universal method to limit the irregularly arranged compacted fillers in a specified sealed container and guarantee the upper surface is flat without execute moderate compression operation.
- The final height of numerical models is unable to be artificially determined because the height error need to be controlled within the allowable range by constantly fine-tuning the particle number of mortar phase.

In this paper, the final sizes of the models are $\Phi 72.0 \text{ mm} \times 155.6 \text{ mm}$ and $\Phi 72.0 \text{ mm} \times 155.4 \text{ mm}$ respectively for Group CA and Group CB. The two groups of concrete specimens have different mix proportions and the parameters of each component are shown in Table 2.

Obviously, according to Table 2, an aggregate can be represented by a clump only when its particle size is larger than 8.0 mm because the minimum particle size of the clump internal structure sphere is 1.8 mm (maximum allowable overlap is 0.675 mm). If an aggregate is too small, the shape precision of its corresponding clump will be greatly reduced and the particle size will be inevitably lower than the actual value. As we know, the mortar is a mixture of sand and set cement. But here we treat it as one component for the consideration of computational efficiency. However, as you can see, we haven’t given the specific volume fraction of the mortar in Table 2 because it is impossible to be as dense as the real mortar. The deviation of the void ratio seems to be a serious problem that can not be ignored. But it is worth mentioning that the UBM is based on the MPB, the partial void between the particles can be considered to be filled with those

Table 1 Shape parameters of typical clusters before scaling.

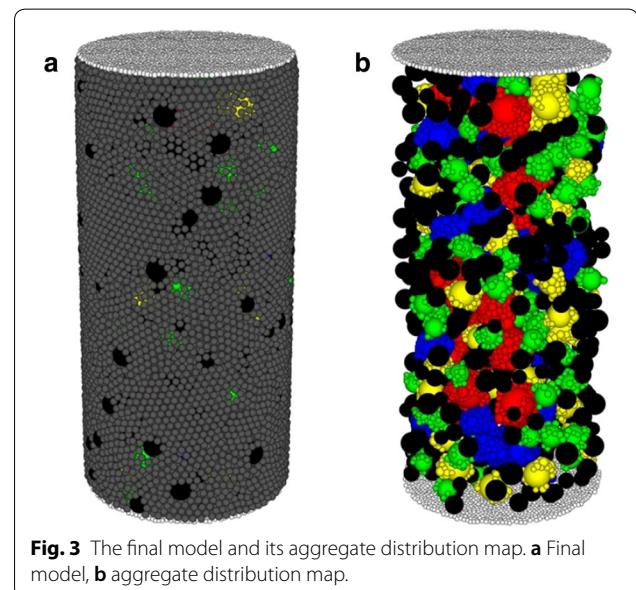
Types of clusters	Shape parameters				
	Size [size (length (mm) × width (mm) × height (mm))]	Number of internal structure spheres	Coefficient of irregularity	Angularity	Surface texture depth (mm)
A	15.27 × 14.00 × 12.73	106	1.832	1.527	0.379
B	13.09 × 12.00 × 10.91	72	1.910	1.548	0.403
C	10.91 × 10.00 × 9.09	39	1.698	1.550	0.461
D	8.73 × 8.00 × 7.27	20	1.613	1.530	0.396

Table 2 Parameters of each component.

Group	Names of component	Volume fraction(%)	Minimum particle size (mm)	Maximum particle size (mm)	Corresponding clump type
CA	Aggregate component 1	7.058	14.00	16.00	A
	Aggregate component 2	7.058	12.00	14.00	B
	Aggregate component 3	7.058	10.00	12.00	C
	Aggregate component 4	7.057	8.00	10.00	D
	Mortar and voids	11.469	4.75	8.00	
CB	Aggregate component 1	7.353	14.00	16.00	A
	Aggregate component 2	7.353	12.00	14.00	B
	Aggregate component 3	7.353	10.00	12.00	C
	Aggregate component 4	7.353	8.00	10.00	D
	Mortar and voids	11.948	4.75	8.00	
	Mortar and voids	58.640	2.66	2.66	

abstract parallel bonds which are able to transmit both forces and moments. In this way, as long as the parallel bond radius and other parameters are set reasonably, the influence of void ratio on the meso mechanical behaviors of concrete can be significantly decreased. The advantage is also the reason why the theory of parallel bond is often used to simulate some dense materials (Tan et al. 2015; Azevedo and Lemos 2013) and it has been confirmed that the parallel bonds are quite proper to model the hydrated cement paste around the aggregates (Lian et al. 2011b; Azevedo 2008; Azevedo et al. 2010; Haeri and Sarfarazi 2016). The final model (just take Group CA for example) and its aggregate distribution map are shown in Fig. 3a, b respectively. Specifically, Fig. 3a shows a complete concrete cylinder specimen model, which contains aggregate particles, mortar particles (whose color is gray) and “ball-walls” (whose color is white). Figure 3b shows its corresponding internal aggregate distribution map, which only contains aggregate particles and “ball-walls”. The total particle numbers of the final models are 39,208 and 38,994 respectively for Group CA and Group CB. The total contact numbers (excluding internal contacts of clumps) of the final models are about 3.8 times as much

as the corresponding particle numbers, namely 150,659 and 147,020.



3 Assignment of the Mesoscopic Mechanical Parameters

3.1 Contact Constitutive Relation and Failure Criterion of the UBM

The overall mechanical behaviors of a material is simulated in PFC^{3D} by associating the constitutive relation and failure criterion with each contact. The so-called constitutive relation consists of four parts:

- An relation between the contact force and relative linear displacement.
- An relation between the contact moment and relative angular displacement.
- An relation between normal and shear contact forces which permits the two contact balls to have a relative slip.
- Residual strength theory for bonds which belong to the non-ITZs.

The failure criterion serves to limit the maximum tensile, compressive and shear stresses of a contact. Alternate constitutive relation and failure criterion are also available by loading the subprogram provided by user themselves into PFC^{3D} and this way is adopted in this paper for creating a new model.

As has been stated above, the UBM is based on the MPB which has a more complex failure criterion compared with the built-in parallel bond (BPB) (Minneapolis 2005). As we know, a BPB is defined by the following five parameters: normal and shear stiffnesses (\bar{k}_i^n and \bar{k}_i^s [stress/displacement]); normal and shear strengths ($\bar{\sigma}$ and $\bar{\tau}$ [stress]); and bond radius \bar{R} . It will be broken when the normal or shear forces exceed their corresponding strengths. Obviously, the tensile strength is equal to the compressive strength by default and they are characterized by using the same parameter $\bar{\sigma}$ which can not unify the loading conditions of tension and compression correctly. What's more, the shear strength shouldn't be a fixed value because it is affected by the normal force. The MPB, however, is defined by the following seven parameters: normal and shear stiffnesses (\bar{k}_i^n and \bar{k}_i^s [stress/displacement]); tensile and compressive strengths ($\bar{\sigma}_t$ and $\bar{\sigma}_c$ [stress]); cohesive force and interior friction angle (c [stress] and φ [degree]) and bond radius \bar{R} which is designated as the geometric mean of the two adjacent particle radii in this paper (see Eq. (1)). The reason why we don't use the arithmetic mean is that it can't well reflect the geometric relation for such a geometric quantity, bond radius.

$$\bar{R} = \sqrt{R^{[A]} \cdot R^{[B]}} \quad (1)$$

Apart from having a more elaborate failure criterion, the MPB is also different from the BPB on the matter

whether it can coexist with the linear-stiffness model. As mentioned above, we treat mortar matrix as one component. However, it doesn't agree with the homogeneity because the stiffness in the overlapping part between a BPB and its corresponding contact entities will be double counted, which will certainly lead to an unreasonable bigger overall stiffness composed of two parts (parallel-bond stiffness and linear contact stiffness). Instead, the existence of a MPB will preclude the possibility of the linear-stiffness model. As to the relation between normal and shear contact forces, a slip model is defined in this paper and the slip condition will be judged by Eqs. (2) and (3). Moreover, the BPB and the behavior of relative slip can occur simultaneously while the MPB will preclude the possibility of the slip model and the latter takes into consideration the quasi-brittle characteristic of mortar matrix which makes it much closer to the real situation.

$$F_{max}^s = \mu |F_i^n|, \quad \text{compressive state} \quad (2)$$

$$\begin{cases} |F_i^s| > F_{max}^s, & \text{relative slip condition} \\ |F_i^s| \leq F_{max}^s, & \text{relative static condition} \end{cases} \quad (3)$$

where μ [dimensionless] is taken to be the static friction coefficient of the two contact entities; F_i^n and F_i^s denote the normal and shear components of contact force vector, respectively; and F_{max}^s is the maximum allowable shear contact force.

When the MPB breaks, the linear-stiffness theory which assumes that the stiffnesses of the two contact entities act in series is adopted in the UBM. The contact normal secant stiffness and shear tangent stiffness (k_i^n and k_i^s [force/displacement]) is given by Eqs. (4) and (5).

$$k_i^n = \frac{k_n^{[A]} k_n^{[B]}}{k_n^{[A]} + k_n^{[B]}} \quad (4)$$

$$k_i^s = \frac{k_s^{[A]} k_s^{[B]}}{k_s^{[A]} + k_s^{[B]}} \quad (5)$$

where the superscripts [A] and [B] denote the two entities in contact; k_n and k_s are the normal and shear stiffnesses [force/displacement] for an entity.

The contact stiffnesses relate the contact forces and relative displacements in the normal and shear directions via Eqs. (6) and (7).

$$F_i^n = k_i^n U^n n_i \quad (6)$$

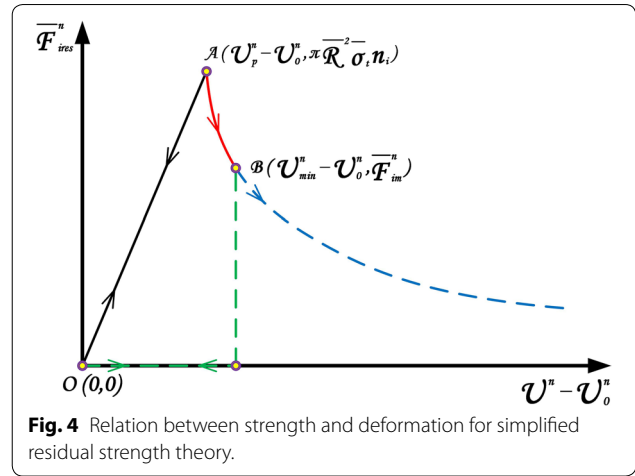
$$\Delta F_i^s = -k_i^s \Delta U^s \quad (7)$$

where U^n [scalar] is the sphere overlap (positive; negative, for a gap) in the normal direction and n_i denote a unit-normal vector on a contact plane. ΔU^s is the shear component of a contact displacement-increment vector which is used to calculate the shear force-increment vector ΔF_i^s .

As you can see, the theory of elastic mechanics is employed to describe the behaviors of contact bonds before them break. If we don't take the residual strengths into consideration, the macroscopic stress-strain responses obtained by simulation are bound to be more brittle than the laboratory measurements. In order to solve this problem, Gitman et al. (2008) adopted an elasticity-based gradient damage model which is able to consider the residual tensile strength on mesoscopic scale. Even though this model is fine, but there are too many empirical parameters need to be designated, namely length-scale parameter ℓ , residual stress parameter $\tilde{\alpha}$ and slope of softening $\tilde{\beta}$. Another model (called isotropic damage model) adopted by He et al. (2011) has a different definition for damage parameter ϖ . Compared with the former, their damage model just have two empirical parameters, namely the width of damage zone \mathfrak{R} and a parameter \tilde{h} related to element size. However, the above two models are all based on the finite element method (FEM) and it is not easy to determine the values of those empirical parameters in 3D discrete element models. Inspired by their damage models, we developed a simplified residual strength theory which is based on power function and only one empirical parameter is needed. With regard to this theory, the relation curve for strength and deformation is shown in Fig. 4. The red, green and blue lines in Fig. 4 represent the possible change paths of bond residual strength with deformation, while the black line stands for the elastic behavior before the corresponding bond cracks. Suppose the tensile deformation of a bond continues to increase to the state of arbitrary point B in Fig. 4, there would be two possible circumstances:

- Providing that the tensile deformation begins to decrease, the state point immediately changes into the path represented by the green line.
- Providing that the tensile deformation continues to increase, the state point gets into the path represented by the blue line.

It is worth mentioning that this simplified residual strength theory will come into play only when the tensile failure occurs for a bond which belongs to the non-ITZs. The residual normal force \bar{F}_{ires}^n carried by the MPB is calculated through Eq. (8).



$$\bar{F}_{ires}^n = \begin{cases} 0, & U_{min}^n \leq U^n < U_0^n \\ \pi \bar{R}^2 \bar{\sigma}_t n_i \left(\frac{U^n - U_0^n}{U_p^n - U_0^n} \right)^{-\bar{\delta}}, & U^n < U_{min}^n \end{cases} \quad (8)$$

where U_0^n is the initial sphere overlap (positive; negative, for a gap), U_p^n is the sphere overlap when the bond reaches its tensile strength $\bar{\sigma}_t$ and U_{min}^n is the minimum sphere overlap which the bond has ever reached. The attenuation coefficient $\bar{\delta}$ of residual strength will be an empirical constant (0.7 for models in this paper) if models are built under the same meso scale. Compared with the non-ITZs, the damage paths of ITZs are relatively fixed and the attenuation coefficient $\bar{\delta}$ will be more greater. For simplicity, the residual strengths of ITZs have been ignored in this paper. In addition, the residual shear force \bar{F}_{ires}^s carried by the MPB is calculated through Eqs. (9) and (10) when the tensile failure occurs for a bond which belongs to the non-ITZs.

$$\bar{F}_{ires}^s = \wp \bar{F}_i^s \quad (9)$$

$$\wp = \begin{cases} 1, & \text{if } |\bar{F}_i^s| \leq \frac{\bar{\tau} |\bar{F}_{im}^n|}{\bar{\sigma}_t} \\ \frac{\bar{\tau} |\bar{F}_{im}^n|}{\bar{\sigma}_t |\bar{F}_i^s|}, & \text{if } |\bar{F}_i^s| > \frac{\bar{\tau} |\bar{F}_{im}^n|}{\bar{\sigma}_t} \end{cases} \quad (10)$$

where \bar{F}_i^s is shear force and \bar{F}_{im}^n denotes the corresponding normal force of minimum sphere overlap U_{min}^n . Likewise, \bar{k}_{im}^n denotes its corresponding normal stiffnesses which will be used in the calculation of bending moment.

$$\bar{k}_{im}^n = \frac{|\bar{F}_{im}^n|}{\pi \bar{R}^2 (U_0^n - U_{min}^n)} \quad (11)$$

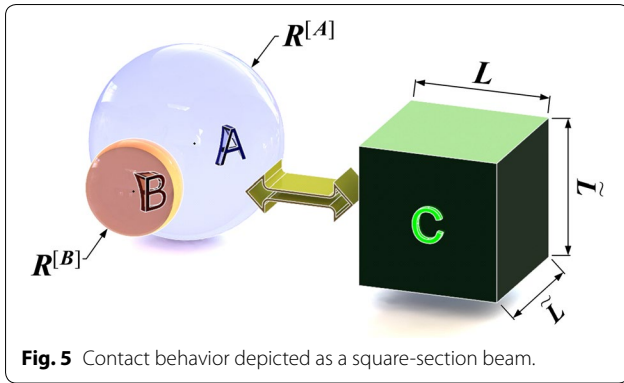


Fig. 5 Contact behavior depicted as a square-section beam.

3.2 Relation Between Macro- and Meso-Properties

The material macroscopic responses can be determined by their corresponding set of deformability and strength parameters of the mesoscopic structures. The behavior of a contact between two particles can be considered as an elastic square-section beam with its ends at the particle centers and this idea is illustrated in Fig. 5. The length L as well as the cross-sectional length \tilde{L} of the beam can be expressed as the average of the two particle diameters, then the cross-sectional area of the beam is given by Eq. (13):

$$L = \tilde{L} = R^{[A]} + R^{[B]} \tag{12}$$

$$A = \tilde{L}^2 \tag{13}$$

The two particles will have the same normal and shear stiffnesses (k_n and k_s) if they belong to the same material and their radii are equal. Then the contact normal and shear stiffnesses are found, using Eqs. (14) and (15), to be:

$$k_i^n = \frac{k_n}{2} \tag{14}$$

$$k_i^s = \frac{k_s}{2} \tag{15}$$

For pure normal and pure shear loading, the normal and shear behaviors are uncoupled and that means the k_i^n and k_i^s also can be expressed as the following equations if the Young's modulus E and the Poisson's ratio ν of the material are known to us. The derivation process of the two formulas are similar to Azevedo's relevant literature (Azevedo 2008; Azevedo et al. 2010).

$$k_i^n = \frac{EA}{L} \tag{16}$$

$$k_i^s = \frac{EA}{2(1 + \nu) \cdot L} \tag{17}$$

Two expressions for k_n and k_s can be obtained by substituting Eqs. (12), (13), (14) and (15) into Eqs. (16) and (17), then rearranging them:

$$k_n = 4ER \tag{18}$$

$$k_s = \frac{2ER}{1 + \nu} \tag{19}$$

where R is the radius of the sphere whose stiffness parameters remain to be assigned.

The behavior of the MPB in this paper is similar to an elastic circular-section beam whose length, \bar{L} in Fig. 6, approaches zero. Relative motion causes normal and shear forces (\bar{F}_i^n and \bar{F}_i^s , respectively) as well as bending and torsional moment (\bar{M}_i^n and \bar{M}_i^s , respectively) to develop. Before the MPB is destroyed, we use a circular-section beam model. Once the MPB is damaged, a rectangular beam model (see Fig. 5) will be activated.

As we know, the concrete is generally considered to be a three-phase composite composed of aggregates, mortar and the ITZs between them. However, as the weakest link in the concrete, it has been recognized that the ITZs (aggregate–aggregate, aggregate–mortar) play a crucial role in the macro-properties of the concrete due to its higher porosity, lower Young's modulus and lower tensile strength compared with the mortar (Shuguang and Qingbin 2015).

For pure normal and pure shear loading, the normal and shear behaviors are uncoupled and the normal and shear stiffnesses of the MPB (\bar{k}_i^n and \bar{k}_i^s , respectively) can be expressed as the following equations:

$$\bar{k}_i^n = \frac{k_i^n}{A} = \begin{cases} \frac{E}{\bar{L}}, & \text{for the mortar-mortar} \\ \frac{\xi \cdot E}{\bar{L}}, & \text{for the ITZs} \end{cases} \tag{20}$$

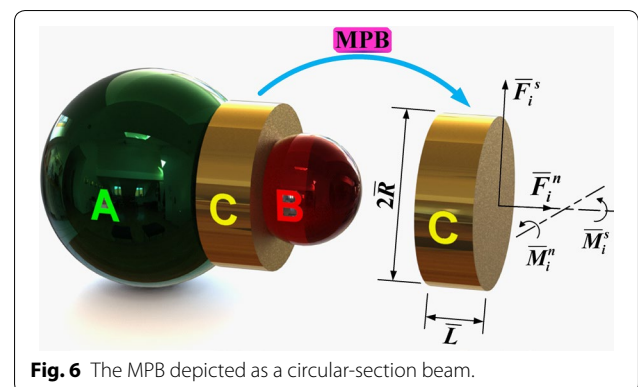


Fig. 6 The MPB depicted as a circular-section beam.

$$\bar{k}_i^s = \frac{k_i^s}{A} = \begin{cases} \frac{E}{2(1+\nu)L}, & \text{for the mortar-mortar} \\ \frac{\xi \cdot E}{2(1+\nu)L}, & \text{for the ITZs} \end{cases} \quad (21)$$

where ξ denotes the reduction factor of the Young's modulus for the ITZs and its value can be taken as 0.45 according to the present research achievements (Yang 1998).

The calculation cycle in PFC^{3D} is a timestepping algorithm that requires the repeated application of the law of motion to each particle, a force-displacement law to each contact and a constant updating of wall positions (Minneapolis 2005). This algorithm can recognize the movement and interaction of particles precisely for any time interval (Lian et al. 2011a) and this process is illustrated in Fig. 7. In the software PFC3D, it is worth mentioning that the timestep adjustment is automatic and it is no need to worry about problems such as particle penetration, result distortion and numerical instability caused by those large timesteps. It is one of the main advantages of this software that it can automatically adjust timestep and ensure the convergence of the calculation results. There are several variables, listed in Table 3, need to be accessed by the MPB dynamically which are used to compute the mechanical responses of the UBM during cycling.

Then the normal and shear forces (\bar{F}_i^n and \bar{F}_i^s , respectively) carried by the MPB can be written as:

$$\Delta \bar{F}_i^n = v_n \Delta t \bar{k}_i^n \bar{A} \quad (22)$$

$$\Delta \bar{F}_i^s = v_s \Delta t \bar{k}_i^s \bar{A} \quad (23)$$

Table 3 MPB variables accessed dynamically during cycling.

Variable name	Physical meaning	Approach to access
Δt	Timestep	Supplied by PFC ^{3D}
v_n	Relative normal velocity	Supplied by PFC ^{3D}
v_s	Relative shear velocity	Supplied by PFC ^{3D}
ω	Relative angular velocity ^a	Supplied by PFC ^{3D}
n_i	Contact unit-normal vector ^b	Calculated by the UBM

^a The relative angular velocity supplied by PFC^{3D} adopts degree measure. A conversion coefficient α is designated here for translating the degree into radian and it can be expressed as $\alpha = \pi/180$.

^b Note that the contact unit-normal vector isn't supplied by PFC^{3D} directly, so the authors developed a program to calculate it every certain and appropriate timesteps since the deformation of the UBM is quite slowly.

$$\bar{F}_i^n = - \sum \Delta \bar{F}_i^n \quad (24)$$

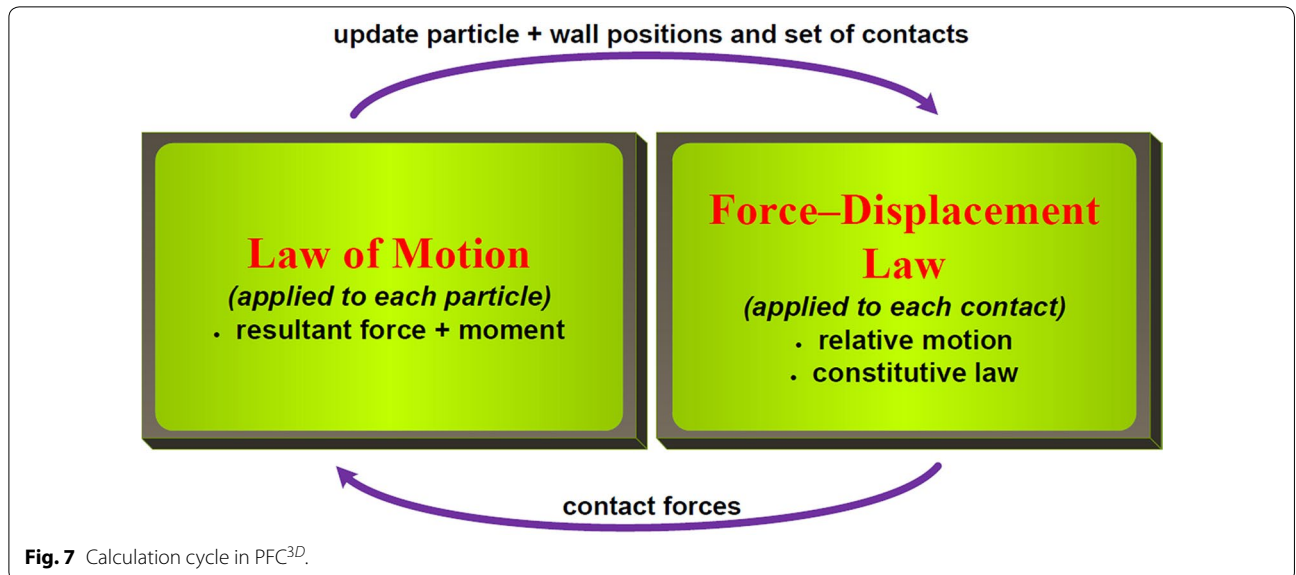
$$\bar{F}_i^s = - \sum \Delta \bar{F}_i^s \quad (25)$$

where $\Delta \bar{F}_i^n$ and $\Delta \bar{F}_i^s$ are the normal and shear force-increment vectors of the UBM respectively; The cross-sectional area of the MPB \bar{A} is given by Eq. (26); The moment and polar moment of inertia (\bar{I} and \bar{J} , respectively) are given by Eqs. (27) and (28):

$$\bar{A} = \pi \bar{R}^2 = \frac{1}{4} \pi (R^{[A]} + R^{[B]})^2 \quad (26)$$

$$\bar{I} = \frac{1}{4} \pi \bar{R}^4 = \frac{1}{64} \pi (R^{[A]} + R^{[B]})^4 \quad (27)$$

$$\bar{J} = 2\bar{I} \quad (28)$$



Then the bending and torsional moment-increment vectors ($\Delta\bar{M}_i^n$ and $\Delta\bar{M}_i^s$, respectively) carried by the MPB can be written as:

$$\zeta_n = (\alpha\omega \cdot n_i) \cdot n_i \tag{29}$$

$$\zeta_s = \alpha\omega - \zeta_n \tag{30}$$

$$\Delta\bar{M}_i^n = \zeta_s \Delta t \bar{k}_i^n \bar{I} \tag{31}$$

$$\Delta\bar{M}_i^s = \zeta_n \Delta t \bar{k}_i^s \bar{J} \tag{32}$$

where ζ_n and ζ_s denote the normal and shear component vectors of the relative angular velocity [radian measure]; The total moment associated with the MPB can be expressed as \bar{M}_i via:

$$\bar{M}_i = - \sum (\Delta\bar{M}_i^n + \Delta\bar{M}_i^s) \tag{33}$$

Local non-viscous damping, to dissipate the excessive kinetic energy by effectively damping the equations of motion, is available in PFC^{3D}. $F_{(i)}^d$ is the damping force:

$$F_{(i)}^d = -\gamma \cdot |\mathcal{F}_{(i)}| \cdot \text{sign}(\mathcal{V}_{(i)}), \quad i = 1 \cdots 6 \tag{34}$$

where $\mathcal{F}_{(i)}$ is the resultant force (the sum of all externally applied forces acting on the particle) and it is controlled by the damping constant γ whose value can be chosen as 0.08 (Nitka and Tejchman 2015). Moreover, $\text{sign}(\bullet)$ denotes the sign function and $\mathcal{V}_{(i)}$ is the generalized velocity given by Eq. (35).

$$\mathcal{V}_{(i)} = \begin{cases} \dot{x}_{(i)}, & \text{for } i=1 \cdots 3 \\ \psi_{(i-3)}, & \text{for } i=4 \cdots 6 \end{cases} \tag{35}$$

where $\dot{x}_{(1)}$, $\dot{x}_{(2)}$ and $\dot{x}_{(3)}$ are the translational velocities referred to the principal axes and $\psi_{(1)}$, $\psi_{(2)}$ and $\psi_{(3)}$ are the angular velocities about the principal axes.

Frankly, the damping constant γ whose value is generally taken as 0.08 (Kozicki et al. 2012, 2014; Nitka and Tejchman 2015) has a little influence on the stress–strain responses in our paper no matter under tension or compression loading condition. According to our research, the peak stress deviations (< 1 MPa for compression; < 0.1 MPa for tension) are almost negligible. Because the loading speed in our article is much smaller than the loading speed in literature (Kozicki et al. 2012, 2014; Nitka and Tejchman 2015) especially for the tensile loading, there is little excess kinetic energy needed to be dissipated so that the effect of local nonviscous damping is not very significant. And this phenomenon has also been emphasized in the literature (Kozicki et al. 2014). The tensile, compressive and shear strengths of the MPB ($\bar{\sigma}_t$, $\bar{\sigma}_c$ and $\bar{\tau}$, respectively) have a one-to-one correspondence

with the material strengths (σ_t , σ_c and τ , respectively) since they are specified in stress units (see Table 4 for details).

where λ denotes the reduction factor of the strength for the ITZs and the value of λ_1 can be specified as 0.45 according to the current research results (Hongyi 2015; Azevedo 2008; Gu et al. 2013; Nagai et al. 2005). The average value of λ_1 in these literature are basically within the range [0.4, 0.5]. Considering the effect of water cement ratio and joint roughness coefficient (JRC), we finally specified it as 0.45 by querying the provided experience curve in the dissertation (Hongyi 2015). Assuming that the ratio of the tensile strength, compressive strength and cohesive force remains unchanged, the values of λ_2 and λ_3 should be the same as that of λ_1 . Besides, the coefficient of strength variation \aleph_s and the coefficient of modulus variation \aleph_e also have been introduced into our models and their values are all 3%.

Unlike the BPB, the shear strength of a MPB isn't a fixed value and Mohr–Coulomb criterion is chosen to calculate its shear strength dynamically as shown in Eq. (36).

$$\bar{\tau} = c + \bar{\sigma} \tan\varphi \tag{36}$$

The cohesive force c can be measured by direct shear test and the typical value of interior friction angle φ can be taken as 35° according to the relevant literature (Xianglin Gu et al. 2013).

4 Tests of Numerical Model and Physical Model

4.1 Tests of Numerical Model

4.1.1 Acquisition of Macroscopic Parameters

The mortar component in the concrete specimen consists of ordinary portland cement, water and sand (fineness modulus fluctuates between 2.3 and 3.0). The corresponding mass ratios of them are 1 : 0.68 : 2.59 and 1 : 0.49 : 1.50 respectively for Group MA and Group MB. The macroscopic tensile, compressive strengths and cohesive force are able to be obtained through the tensile test, compressive test and direct shear test respectively. Specifically speaking, the testing methods and facilities for the tensile and compression tests of the mortar specimens are similar to those used in the corresponding concrete tests. The size of the mortar specimens is 40 mm × 40 mm × 40 mm (*length × width × height*)

Table 4 Mesoscopic strength parameters of the MPB.

Zone	Tensile strength	Compressive strength	Cohesive force strength
ITZs	$\lambda_1 \cdot \sigma_t$	$\lambda_2 \cdot \sigma_c$	$\lambda_3 \cdot c$
Mortar–mortar	σ_t	σ_c	c

for compression and $40\text{ mm} \times 40\text{ mm} \times 160\text{ mm}$ (*length* \times *width* \times *height*) for tension. The reason why we measured the macroscopic tensile strength by uniaxial tensile test is that uniaxial tensile strength is more reliable than other tensile strengths (Haeri et al. 2016; Sarfarazi and Schubert Sarfarazi and Schubert). With regard to the direct shear test of mortar specimens, the traditional rectangular short-beam direct shear test is adopted. As we know, the traditional rectangular short-beam direct shear test is the most commonly used method of direct shear test owing to its simple and intuitive design, which was first put forward and adopted by a German scholar Mörsch. During the test, both ends of a specimen were supported by two rigid plates. Then the mid-span load is applied to the rectangular short-beam through the upper rigid plate until it is destroyed and the size of the mortar specimens is $120\text{ mm} \times 40\text{ mm} \times 40\text{ mm}$ (*length* \times *width* \times *height*). The experimental results are as follows: Group MA: $\sigma_t = 3.02\text{ MPa}$, $\sigma_c = 31.3\text{ MPa}$ and $c = 9.73\text{ MPa}$; Group MB: $\sigma_t = 4.17\text{ MPa}$, $\sigma_c = 52.2\text{ MPa}$ and $c = 16.7\text{ MPa}$. Notice that Group MA and Group MB are the corresponding mortar phase specimens of Group CA and Group CB respectively.

The aggregates in the concrete specimen are all crushed basalt whose joint roughness coefficient (JRC) is about 7.0. The approximate density value of the basalt and the mortar (ρ_a and ρ_m , respectively) can be measured by the Archimedes method. Other parameters such as friction coefficient μ , Young's modulus E (The HS-bounds method (Simeonov and Ahmad 1995) is taken here and the average value of HS-bounds is used to estimate the Young's modulus of the mortar phase) and Poisson's ratio ν can be gained by consulting relevant literature (Franz et al. 2003; Richard 1993; Simeonov and Ahmad 1995; Schultz 1995) and their specific values adopted in this paper are listed in Table 5.

4.1.2 Loading Mechanism

PFC^{3D} only allows particles to be bonded together at contacts, a particle may not be bonded to a wall. That is to say, it's necessary to use the "ball-walls" composed of some sphere particles whose radii are 0.9 (maximum

allowable overlap is 0.45 mm) to simulate the condition of tension and the "ball-walls" are defined as clumps.

During the loading process, the strain of a specimen is captured by monitoring the Z coordinate variations of the contacts existing in the loading boundaries. It is assumed that the stiffness of the "ball-walls" is far greater than that of the specimens for the purpose of reducing the post-peak springback of the "ball-walls" and facilitating the post-peak speed control of loading.

For the condition of tension, each contact between the "ball-walls" and the surfaces (top and bottom) of specimens is assigned with a MPB whose strength and stiffness are all far greater than those within the specimens in order to guarantee that it won't crack and the post-peak springback of a MPB can be ignored so that the post-peak loading speed can't be seriously affected by the rebound velocity of the MPB. The loading mode is uniaxial symmetrical tension.

By contrast, there are no bond exist in the interfaces between the "ball-walls" and the surfaces (top and bottom) of specimens in the condition of compression. The friction coefficient of the "ball-walls" μ_w is consistent with that of the real loading plates, namely $\mu_w = 0.15$. The loading mode is uniaxial symmetrical compression.

It is necessary to control the reasonable loading speed to ensure a quasi-static equilibrium (for discrete models, literature (Haeri and Sarfarazi 2016; Sarfarazi et al. 2014; Ghazvinian 2012) suggest that 0.016 m/s will be an appropriate loading speed while literature (Kozicki et al. 2014, 2012) suggest that 0.010 m/s will be an appropriate loading speed). The large-scale computing device provided by the Research Institute of Hydraulic Structure (Hohai University) allows us to further reduce the loading speed to 0.00025 m/s for uniaxial symmetrical tension and 0.0025 m/s for uniaxial symmetrical compression. Therefore the loading speed is slow enough to ensure the tests are conducted under quasi-static conditions. Roughly speaking, the corresponding simulation times for tension and compression tests in our paper are all about 10 days (parallel-processing mode is off).

4.2 Tests of Physical Model

After those two groups of concrete specimens (Group CA and Group CB) were manufactured and formed, they were instantly placed in a suitable environment ($20 \pm 5^\circ\text{C}$) and kept for 1 day, then they were moved to the standard curing room ($20 \pm 2^\circ\text{C}$ for temperature and 95% for relative humidity) and kept for 28 days.

Each group of concrete specimens was planned to be used for two kinds of experiments, namely uniaxial tensile and compressive tests. MTS material testing system (as shown in Fig. 8a) and WAW microcomputer control electro-hydraulic servo testing machine (as shown in

Table 5 Relevant macroscopic mechanical parameters.

Parameters	Aggregate	Mortar
Density (kg/m^3)	2680	2200
Friction coefficient	0.60	1.02
Young's modulus (GPa)	73.0	20.4 (for Group CA) 25.9 (for Group CB)
Poisson's ratio	0.25	0.20

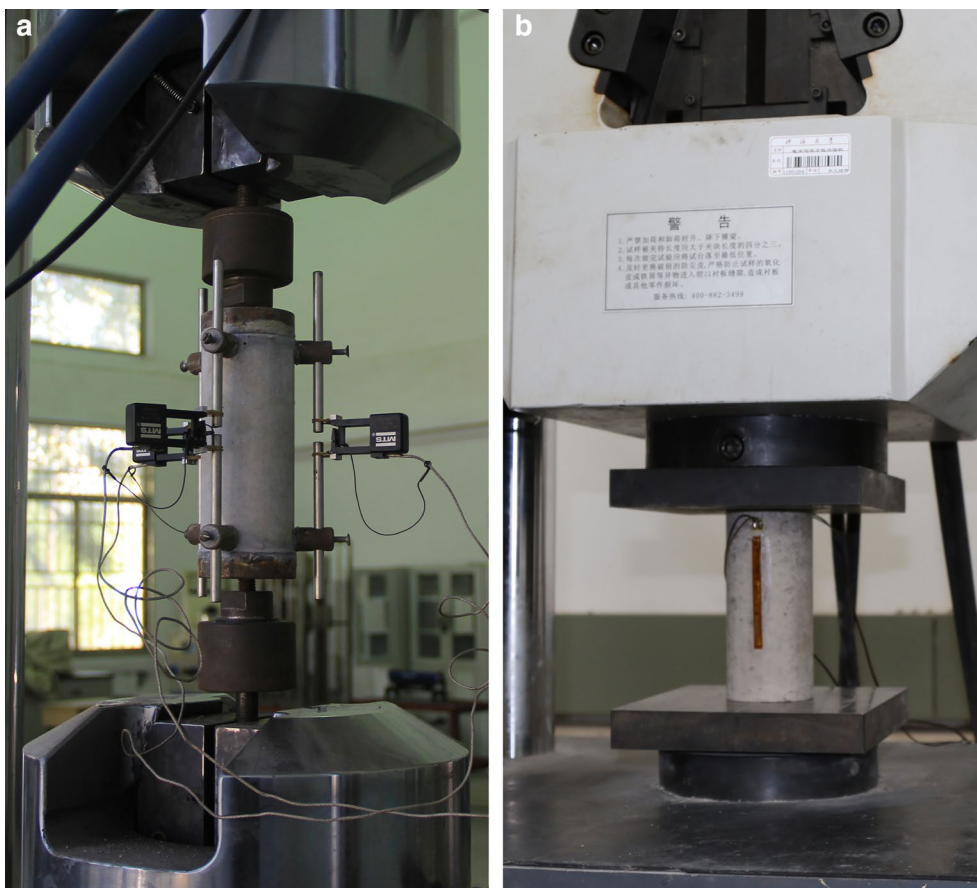


Fig. 8 Testing devices. **a** MTS material testing system, **b** WAW testing machine.

Fig. 8b) are available for the uniaxial tensile and compressive tests respectively. Three extensometers are used for every tensile specimen to measure the axial tensile strain, while two strain gages are symmetrically arranged in the cylindrical surface of every compressive specimen to measure the axial compressive strain.

A kind of epoxy resin structural adhesive (bond tensile strength is about 10 MPa) is applied to cohere the loading plates ($\Phi 72 \text{ mm} \times 20 \text{ mm}$) and the ends of specimens before the uniaxial tensile tests. The pull rods fixed on loading plates should be connected with the fixtures of the MTS material testing system. It's also essential to adjust the tightness degree of connecting bolts in the pull rods and align the pull rods and the central axis of a specimen as accurately as possible.

5 Comparison of Numerical and Experimental Results

5.1 Failure Patterns Under Different Loading Conditions

The typical failure patterns of the laboratory tests under tensile and compressive loading conditions are shown in

Fig. 9a, b) respectively. Obviously, the typical failure pattern of concrete specimen in laboratory uniaxial tensile test is that the specimen has been divided into two parts

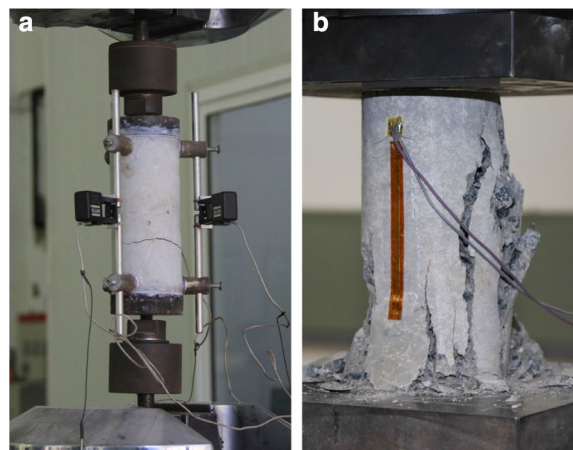


Fig. 9 Typical failure patterns of the laboratory tests. **a** Typical failure pattern under tension, **b** typical failure pattern under compression.

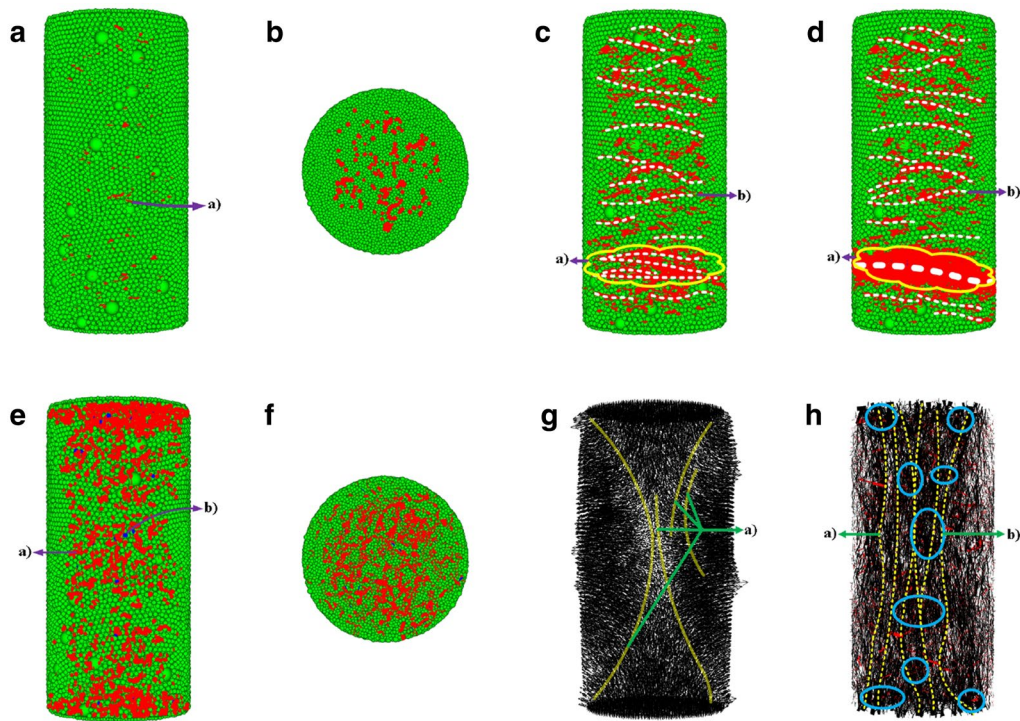


Fig. 10 Crack development of specimens at different loading stages. **a** The state of crack propagation under tension. **a)** Represents normal failure of a bond, **b** the state of crack propagation under tension (top view), **c** the state of peak strain under tension. **a)** and **b)** Represent the locations of main failure faces and other failure faces, respectively, **d** the state of triple peak strain under tension. **a)** and **b)** Represent the locations of main failure faces and other failure faces, respectively, **e** the state of crack propagation under compression. **a)** and **b)** Represent normal and shear failure of a bond, respectively, **f** the state of crack propagation under compression (top view), **g** the state of triple peak strain under compression (displacement vector diagram). **a)** Represents the main fault zones, **h** the state of triple peak strain under compression (Force chains diagram). **a)** and **b)** Represent the main load-transferred paths and the stress concentration zones, respectively.

and its only main failure face is approximately parallel to the loading boundaries. In contrast, the typical failure pattern of concrete specimen in laboratory uniaxial compressive test is that there are several main fault zones have been formed and almost all of them are approximately perpendicular to the loading boundaries. As a comparison, the failure patterns of the numerical simulation can be illustrated and characterized mainly by two ways, namely crack tracking method and displacement nephogram method, respectively. Furthermore, two additional ways, displacement vector diagram method and force chains diagram method, are necessary to be combined used in order to reflect the failure process of concrete more comprehensively.

Just take Group CA for example, for the former main approach (crack tracking method), the damage formation throughout the tensile specimen can be seen in Fig. 10a through Fig. 10d, which depict the cracking mode such as the orientation, location and type (red and blue correspond to normal failure and shear failure, respectively) of each microcrack at different deformation stages.

During the tensile loading process, microcracks initiated randomly, then formed several failure faces perpendicular to the loading direction. With the increase of tensile deformation, some failure faces became the main failure face and eventually led to complete fracture of the tensile specimen.

Nevertheless, it is inappropriate for the crack tracking method to reflect the whole process of compressive specimen's damage formation due to the excessive microcracks showed in the model so that it is difficult to recognise the main fault zones. Therefore, the displacement vector diagram and force chains diagram are adopted to show its damage formation at the state of triple peak strain (see Fig. 10e through Fig. 10h). During the compressive loading process, microcracks also initiated randomly, then a series of main fault zones were formed with the increase of compressive deformation and eventually ran through the compressive specimen. What's more, a measurement of the damage formation is shown in Fig. 11, which depicts the total number of microcracks (broken bonds) as well as the corresponding normal

and shear failure numbers versus axial strain. It should be noted that the meaning of crack propagation point in this paper is the relatively obvious inflection point which connects the slow and rapid increase stages of the total number of microcracks rather than the state when the first microcrack appears (crack initiation defined in mesoscopic level). Obviously, for mesoscopic level, crack propagation has more practical significance compared with crack initiation. We can see it clearly that the total number of microcracks has a tendency of exponential growth after crack propagation point and finally tended to be gentle after peak strain point.

For the latter main approach (displacement nephogram method), the damage formation throughout the specimens can be seen in Fig. 12a through Fig. 12h, which depict the axial displacement nephograms for tension and radial displacement nephograms for compression at different deformation stages. Obviously, the main failure faces of tensile numerical models and the main fault zones of compressive numerical models are all similar to the failure patterns of the laboratory tests (as shown in Fig. 9). Specifically speaking, Fig. 12a, b as well as Fig. 12e, f reflect the changes of failure faces under tensile loading condition and the main failure faces which present between the red and blue color

regions tend to be parallel with the loading boundaries. It is noteworthy that the main failure faces rapidly developed while the others almost had no changes after reaching the peak stress. Fig. 12c, d as well as Fig. 12g, h reflect the changes of fault zones under compressive loading condition and the main fault zones which roughly present between the yellow and cyan color regions tend to be oriented at an approximate angle range $[0^\circ, 45^\circ]$ to the direction of loading application. In addition, the phenomenon that some longitudinal main fault zones finally reached the loading boundaries is predicted.

5.2 Stress–Strain Responses Under Different Loading Conditions

The predicted stress–strain responses and their comparison with experimental results under tensile and compressive loading conditions are shown in Fig. 13a, b respectively. It is worth mentioning that two complete stress–strain empirical curves (namely the dark green and light green dotted lines in Fig. 13b) under compression drew by a recommended empirical formula (Yiqiang et al. 2005) are used for reflecting the general trend of experimental curves whose downward sections

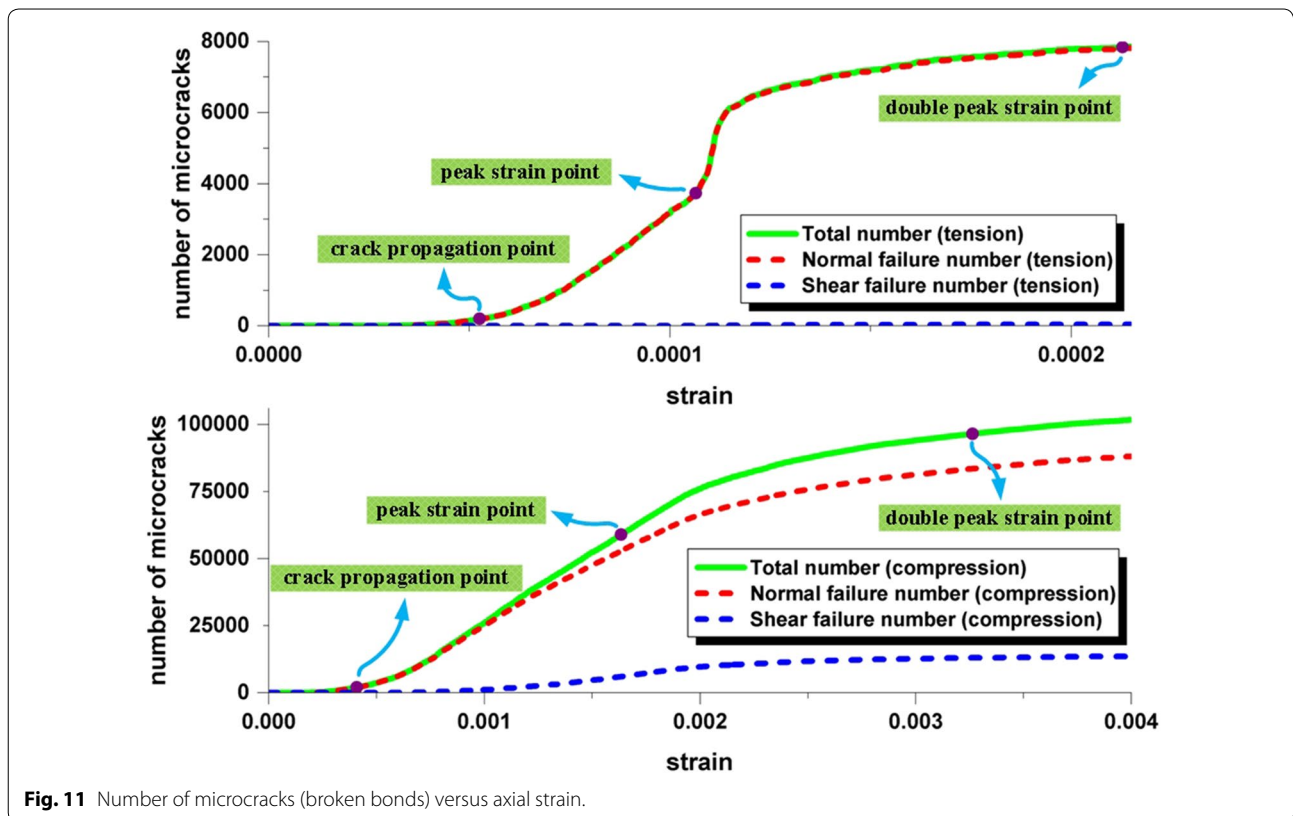


Fig. 11 Number of microcracks (broken bonds) versus axial strain.

are hard to be obtained under the existing experimental conditions. The recommended empirical formula about the stress $\check{\sigma}_c$ and strain ε under compression is as follows:

$$\check{\sigma}_c = \begin{cases} f_p \cdot \frac{\chi \cdot \frac{\varepsilon}{\varepsilon_p} - \frac{\varepsilon^2}{\varepsilon_p^2}}{1 + (\chi - 2) \cdot \frac{\varepsilon}{\varepsilon_p}}, & (0 \leq \varepsilon < \varepsilon_p) \\ f_p \cdot \frac{\frac{\varepsilon}{\varepsilon_p}}{\beta \cdot (\frac{\varepsilon}{\varepsilon_p} - 1)^2 + \frac{\varepsilon}{\varepsilon_p}}, & (\varepsilon \geq \varepsilon_p) \end{cases} \quad (37)$$

Where χ is the coefficient equal to the ratio of initial elastic modulus E_0 to peak secant modulus E_p and the value of it can be taken as 2.0 while the independent parameter β can be taken as 0.8 and 2.0 respectively for Group CA and Group CB according to the literature (Zhenhai 1997). According to the experimental results, the values of axial compressive strength f_p and the

peak strain ε_p can be taken as follows: 24.54 MPa and 1.54×10^{-3} respectively for Group CA; 37.44 MPa and 1.88×10^{-3} respectively for Group CB.

For Group CA, we can find of the simulated and experimental curves have basically similar tendencies and strengths no matter under tension or compression loading condition apart from the smaller peak strain (corresponding to the peak stress) of simulated stress–strain curve. As mentioned above, the residual strength of shear failure for a bond which belongs to the non-ITZs has been ignored, which will inevitably lead to the higher efficiency of energy accumulation for those unbroken bonds in numerical models. Maybe this is the main reason why the peak strain of simulated stress–strain curve is less than the experimental one especially for the compression loading condition. For Group CB, another major difference between the simulated and experimental curves embodies in the slopes of downward sections (also known as softening

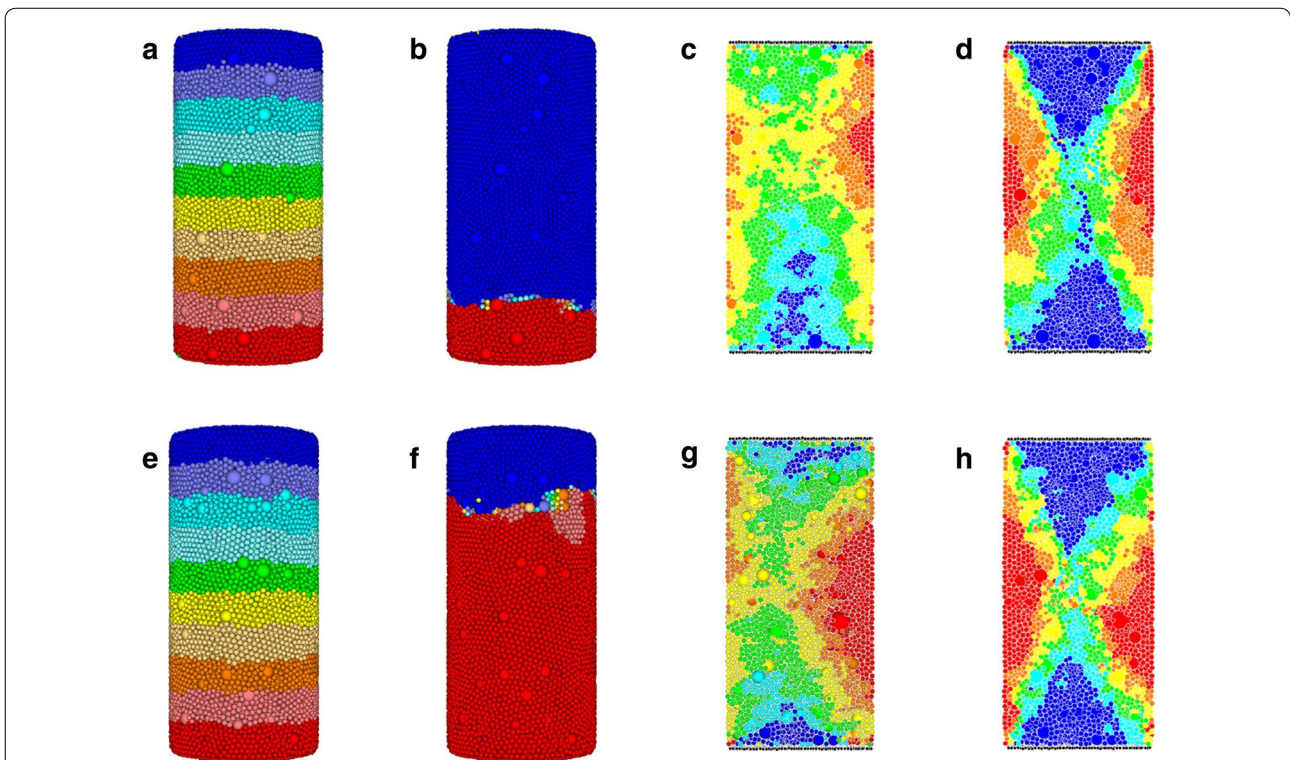
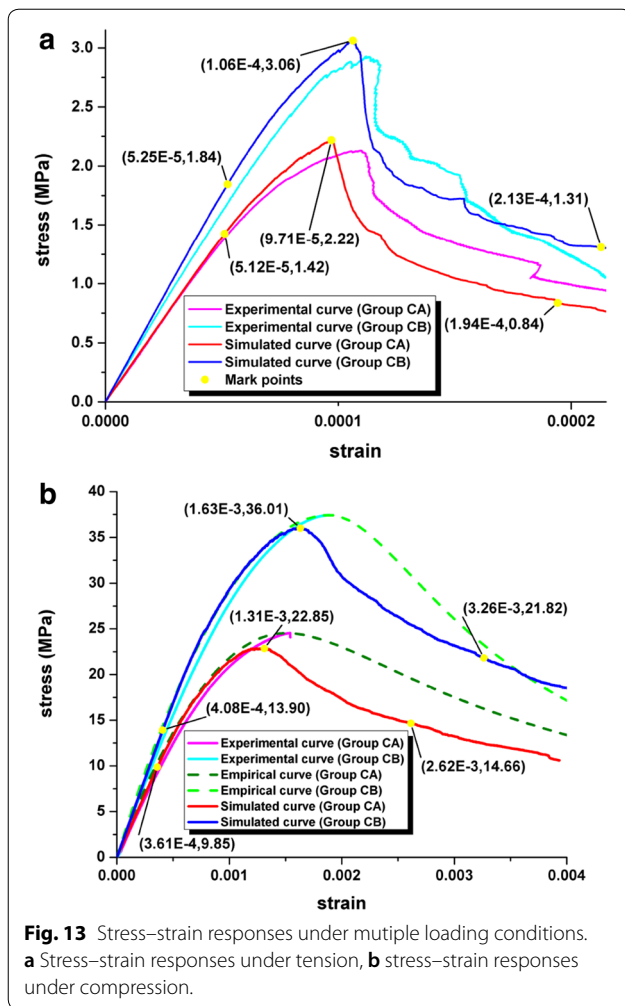


Fig. 12 Displacement nephograms of numerical models at different loading stages. **a** Pre-peak axial displacement nephogram (tension for Group CA). The particle's color will be relatively close to blue while its tensile displacement is relatively large, **b** post-peak axial displacement nephogram (tension for Group CA). The particle's color will be relatively close to blue while its tensile displacement is relatively large, **c** pre-peak radial displacement nephogram (compression for Group CA). The particle's color will be relatively close to red while its radial displacement is relatively large (cutaway view), **d** post-peak radial displacement nephogram (compression for Group CA). The particle's color will be relatively close to red while its radial displacement is relatively large (cutaway view), **e** pre-peak axial displacement nephogram (tension for Group CB). The particle's color will be relatively close to blue while its tensile displacement is relatively large, **f** post-peak axial displacement nephogram (tension for Group CB). The particle's color will be relatively close to blue while its tensile displacement is relatively large, **g** pre-peak radial displacement nephogram (compression for Group CB). The particle's color will be relatively close to red while its radial displacement is relatively large (cutaway view), **h** post-peak radial displacement nephogram (compression for Group CB). The particle's color will be relatively close to red while its radial displacement is relatively large (cutaway view).



branches) both for tension and compression. That the unloading rebound of a bond which is in the state of residual strength has been ignored might be the main reason why the downward slopes of numerical curves are flatter than those of the experimental ones.

What the simulated curves imply is that the stress $\check{\sigma}$ increased approximately linearly at first (the stage before crack propagation point), then a long distinctly nonlinear phase appeared when the crack propagation stress $\check{\sigma}_{pro}$ was reached (the stage between crack propagation point and peak strain point). Afterwards, the curves gradually descended after they got to the peak stress $\check{\sigma}_{max}$ (the stage after peak strain point). As is known to us all, the definition of crack initiation point in macroscopic level is the point where the stress–strain curve begins to be nonlinear. With regard to the experimental curves, the crack initiation (defined in macroscopic level) stress can be roughly taken as 65% of the peak stress for the tensile condition (Feng 2006) while the corresponding stress index can be roughly taken as 40% of the peak stress for

the compressive condition (Zhenhai 1997) (mark points of the experimental curves have been omitted in the graphs). The comparison of relevant stress indexes for those mark points are listed in Table 6.

Strikingly, from the above comparison, the values of crack initiation (defined in macroscopic level) stresses are pretty close to those of crack propagation stresses. In particular, the ratio of crack propagation stress to peak stress are around 0.62 and 0.41% respectively for tension and compression which means the similarity of crack initiation (defined in macroscopic level) stresses and crack propagation stresses is quite high. What's more, the absolute values of peak stress relative errors are all below 7.0% which is within the allowable range. In brief, except for the relevant indexes about the residual stress corresponding to the double peak strain, other characteristic stress values of simulated mark points are all close to the experimental corresponding values no matter under tension or compression loading condition.

6 Discussion and Conclusions

Some meso-level analyses of concrete are carried out by a 3D UBM in this study, which is able to take into account both the geometrical shapes and volume fraction of aggregates simultaneously. What's more, the proposed method can simulate the mechanical behaviors of concrete well to a certain extent no matter under tension or compression loading condition by using the same UBM and the same set of model parameters. Overall, the results of numerical simulation and laboratory tests have basically similar failure patterns and stress–strain responses. The discussion and concluding remarks drawn from this study are listed below:

- In the simulation of uniaxial tensile tests, several failure faces approximately parallel to the loading boundaries were formed (see Fig. 10c) and some of them would become the main failure faces which eventually divided the specimen into two parts (see Fig. 10d). After reaching the peak stress, the main failure faces rapidly developed while the others almost had no changes which can be called disturbed zones (see Fig. 12a, b as well as Fig. 12e, f).
- In the simulation of uniaxial compressive tests, several fault zones approximately perpendicular to the loading boundaries were formed and some of them would become the main fault zones which eventually ran through the specimen (see Fig. 10g, h as well as Fig. 12d, h).
- The total number of microcracks (broken bonds) in a specimen has a tendency of exponential growth after crack propagation point and finally tended to be gentle after peak strain point no matter under tension or

Table 6 Comparison of relevant stress indexes for mark points.

Group	Stress indexes	Uniaxial tensile tests			Uniaxial compressive tests		
		Simulation	Experiment	Relative error (%)	Simulation	Experiment	Relative error (%)
CA	$\check{\sigma}_{ini}$		1.38 MPa	2.9		9.82 MPa	0.3
	$\check{\sigma}_{pro}$	1.42 MPa			9.85 MPa		
	$\check{\sigma}_{max}$	2.22 MPa	2.13 MPa	4.2	22.85 MPa	24.54 MPa	-6.9
	$\check{\sigma}_{res}$	0.84 MPa	0.93 MPa	-9.7	14.66 MPa	17.13 MPa*	-14.4
	$\check{\sigma}_{ini}/\check{\sigma}_{max}$		0.65	-1.5		0.40	7.5
	$\check{\sigma}_{pro}/\check{\sigma}_{max}$	0.64			0.43		
	$\check{\sigma}_{res}/\check{\sigma}_{max}$	0.38	0.44	-13.6	0.64	0.70	-8.6
CB	$\check{\sigma}_{ini}$		1.90 MPa	-3.2		14.98 MPa	-7.2
	$\check{\sigma}_{pro}$	1.84 MPa			13.90 MPa		
	$\check{\sigma}_{max}$	3.06 MPa	2.92 MPa	4.8	36.01 MPa	37.44 MPa	-3.8
	$\check{\sigma}_{res}$	1.31 MPa	0.97 MPa	35.1	21.82 MPa	18.88 MPa	15.6
	$\check{\sigma}_{ini}/\check{\sigma}_{max}$		0.65	-7.7		0.40	-2.5
	$\check{\sigma}_{pro}/\check{\sigma}_{max}$	0.60			0.39		
	$\check{\sigma}_{res}/\check{\sigma}_{max}$	0.43	0.33	30.3	0.61	0.50	22.0

* The value of residual stress corresponding to double peak strain is taken from empirical curve.

compression loading condition (see Fig. 11). Moreover, the curves of corresponding normal and shear failure numbers show that the main failure mode of contact bonds is normal failure no matter under tension or compression loading condition.

- By observing the colors and shapes of the incipient microcracks (see Fig. 10a, e), the authors find there are only red microcracks in the tensile specimen and most of them are transverse fusiform while there are both red and blue microcracks in the compressive specimen and most of them are longitudinal fusiform. This phenomenon indicate that the incipient microcracks are mainly brought about by the normal forces and it can be inferred that their failure modes are tearing-tensile failure and bulging-tensile failure respectively.
- Since the simplified residual strength theory used in our models only applies to the situation when the tensile failure occurs for a bond which belongs to the non-ITZs, the residual strength of shear failure for a bond which belongs to the non-ITZs has been ignored. Consequently, with the increase of the shear failure number in numerical models, the efficiency of energy accumulation for those unbroken bonds in numerical models will be much higher than those in real specimens. Maybe this is the main reason why the peak strain (strain corresponding to the peak stress) of the simulated stress-strain curve is less than the experimental one especially for compression loading condition.
- For the simplified residual strength theory adopted in this paper, the unloading rebound of a bond

which is in the state of residual strength has been ignored, which might be the main reason why the downward slopes of numerical curves are flatter than those of the experimental ones especially for Group CB. Specifically, the higher the strengths are, the relatively flatter the downward slopes of numerical curves will be. Of course, the precondition is that the attenuation coefficient $\check{\sigma}$ of residual strength remains unchanged.

However, the research findings and conclusions in this paper were only based on the two loading conditions, namely tension and compression. Deeper research will be performed in the future for the simulation of more loading conditions such as direct shear test and three-point bending test by using the 3D UBM. Additionally, the feasibility study of the simulation for concrete under combined loading conditions are also ongoing for further validation.

Authors' contributions

JR carried out the experiment, the DEM simulation and drafted the manuscript. ZT supervised the whole study and gave guidances of the study. JB helped with the experiment and the data analysis. All authors read and approved the final manuscript.

Acknowledgements

This study is financially supported by national natural science fund of China (No. 51279054) and the Priority Academic Program Development of Jiangsu Higher Education Institutions in China (No. YS11001). In addition, fruitful discussions about the experiment schemes with Dr. Xudong Chen from Hohai University are acknowledged. Finally, The authors greatly appreciate the necessary support of testing facilities and the large-scale computing device provided by the Research Institute of Hydraulic Structure (Hohai University), Jinling Institute of Technology and the Nanjing Hydraulic Research Institute (NHRI).

Competing interests

The authors declare that they have no competing interests.

Publisher's Note

Springer Nature remains neutral with regard to jurisdictional claims in published maps and institutional affiliations.

Received: 13 May 2017 Accepted: 26 June 2018

Published online: 24 September 2018

References

- Azevedo, N. M., & Lemos, J. V. (2006). Aggregate shape influence on the fracture behaviour of concrete. *Structural Engineering and Mechanics*, 24(4), 411–427.
- Azevedo, N. M., Lemos, J. V., & de Almeida, J. R. (2008). Influence of aggregate deformation and contact behaviour on discrete particle modelling of fracture of concrete. *Engineering Fracture Mechanics*, 75(6), 1569–1586.
- Azevedo, N. M., Lemos, J. V., & Almeida, J. R. (2010). A discrete particle model for reinforced concrete fracture analysis. *Structural Engineering and Mechanics*, 36, 343–361.
- Balevicius, R., Diugys, A., Kaianauskas, R., Maknickas, A., & Visklavicius, K. (2006). Investigation of performance of programming approaches and languages used for numerical simulation of granular material by the discrete element method. *Computer Physics Communications*, 175(6), 404–415.
- Barrett, P. J. (1980). The shape of rock particles, a critical review. *Sedimentology*, 27(3), 291–303.
- Brara, A., Camborde, F., Klepaczko, J. R., & Mariotti, C. (2001). Experimental and numerical study of concrete at high strain rates in tension. *Mechanics of Materials*, 33(1), 33–45.
- Camborde, F., Mariotti, C., & Donz, F. V. (2000). Numerical study of rock and concrete behaviour by discrete element modelling. *Computers and Geotechnics*, 27(4), 225–247.
- Chen, J., Pan, T., & Huang, X. (2011). Discrete element modeling of asphalt concrete cracking using a user-defined three-dimensional micromechanical approach. *Journal of Wuhan University of Technology*, 26(6), 1215–1221.
- Dong, W. E. I., Dong-mei, L. I., & You-qun, H. (2007). Algorithm and implementation of continuous rotation of three-dimensional graphic around coordinate axis. *Journal of Shenyang University of Technology*, 29(6), 696–698.
- Ghazvinian, A., Sarfarazi, V., Schubert, W., & Blumel, M. (2012). A study of the failure mechanism of planar non-persistent open joints using pfc2d. *Rock Mechanics and Rock Engineering*, 45, 677–693.
- Gitman, I. M., Askes, H., & Sluys, L. J. (2008). Coupled-volume multi-scale modeling of quasi-brittle material. *European Journal of Mechanics—A/Solids*, 27(3), 302–327.
- Haeri, H. (2015). Propagation mechanism of neighboring cracks in rock-like cylindrical specimens under uniaxial compression. *Journal of Mining Science*, 51(3), 487–496.
- Haeri, H., & Sarfarazi, V. (2016). Numerical simulation of tensile failure of concrete using particle flow code (PFC). *Computers and Concrete*, 18, 39–51.
- Haeri, H., Sarfarazi, V., & Hedayat, A. (2016). Suggesting a new testing device for determination of tensile strength of concrete. *Structural Engineering and Mechanics*, 60(6), 939–952.
- Haeri, H., Shahriar, K., & Marji, M. F. (2013). Modeling the propagation mechanism of two random micro cracks in rock samples under uniform tensile loading. In *13th International Conference on Fracture 2013* (pp. 16–21).
- Hentschel, M., & Neil, W. (2003). Selection of descriptors for particle shape characterization. *Particle & Particle Systems Characterization*, 20(1), 25–38.
- Hentz, S., Donz, F. V., & Daudeville, L. (2004). Discrete element modelling of concrete submitted to dynamic loading at high strain rates. *Computers & Structures*, 82(2930), 2509–2524.
- He, H., Stroeven, P., Stroeven, M., & Sluys, L. J. (2011). Influence of particle packing on fracture properties of concrete. *Computers and Concrete*, 8(6), 677–692.
- Heukamp, F. H., Ulm, F. J., & Germaine, J. T. (2003). Poroplastic properties of calcium-leached cement-based materials. *Cement and Concrete Research*, 33(8), 1155–1173.
- Hongyi, X. (2015). Experimental study on mechanical properties of composed phases of concrete. Master's thesis. Northwest A&F University. (in Chinese).
- Kaianauskas, R., Maknickas, A., Kaianauskas, A., Markauskas, D., & Balevicius, R. (2010). Parallel discrete element simulation of poly-dispersed granular material. *Advances in Engineering Software*, 41(1), 52–63.
- Kim, H., & Buttlar, W. G. (2009). Discrete fracture modeling of asphalt concrete. *International Journal of Solids and Structures*, 46(13), 2593–2604.
- Kim, H., Wagoner, M. P., & Buttlar, W. G. (2009). Numerical fracture analysis on the specimen size dependency of asphalt concrete using a cohesive softening model. *Construction and Building Materials*, 23(5), 2112–2120.
- Kozicki, J., & Donz, F. V. (2008). A new open-source software developed for numerical simulations using discrete modeling methods. *Computer Methods in Applied Mechanics and Engineering*, 197(4950), 4429–4443.
- Kozicki, J., & Tejchman, J. (2008). Modelling of fracture process in concrete using a novel lattice model. *Granular Matter*, 10(5), 377–388.
- Kozicki, J., Tejchman, J., & Mroz, Z. (2012). Effect of grain roughness on strength, volume changes, elastic and dissipated energies during quasi-static homogeneous triaxial compression using DEM. *Granular Matter*, 14, 457–468.
- Kozicki, J., Tejchman, J., & Muhlhaus, H. B. (2014). Discrete simulations of a triaxial compression test for sand by DEM. *International Journal for Numerical and Analytical Methods in Geomechanics*, 38, 1923–1952.
- Latham, J.-P., Anastasaki, E., & Xiang, J. (2013). New modelling and analysis methods for concrete armour unit systems using FEMDEM. *Coastal Engineering*, 77, 151–166.
- Lemos, V. (2013). A 3D generalized rigid particle contact model for rock fracture. *Engineering Computations*, 30(2), 277–300.
- Lian, C. Q., Yan, Z. G., & Beecham, S. (2011a). Modelling pervious concrete under compression loading a discrete element approach. *Advanced Materials Research*, 168–170, 1590–1600.
- Lian, C., Zhuge, Y., & Beecham, S. (2011b). Numerical simulation of the mechanical behaviour of porous concrete. *Engineering Computations*, 28(8), 984–1002.
- Liu, Y., You, Z., & Zhao, Y. (2012). Three-dimensional discrete element modeling of asphalt concrete: Size effects of elements. *Construction and Building Materials*, 37, 775–782.
- Mechtcherine, V., & Shyshko, S. (2015). Simulating the behaviour of fresh concrete with the distinct element method deriving model parameters related to the yield stress. *Cement and Concrete Composites*, 55, 81–90.
- Minneapolis. (2005). PFC3D (Particle Flow Code in 3 Dimensions), Version 3.1.
- Nagai, K., Sato, Y., & Ueda, T. (2004). Mesoscopic simulation of failure of mortar and concrete by 2D RBSM. *Journal of Advanced Concrete Technology*, 2(3), 359–374.
- Nagai, K., Sato, Y., & Ueda, T. (2005). Mesoscopic simulation of failure of mortar and concrete by 3D RBSM. *Journal of Advanced Concrete Technology*, 3(3), 385–402.
- Nitka, M., & Tejchman, J. (2015). Modelling of concrete behaviour in uniaxial compression and tension with DEM. *Granular Matter*, 17(1), 145–164.
- Piotrowska, E., Malecot, Y., & Ke, Y. (2014). Experimental investigation of the effect of coarse aggregate shape and composition on concrete triaxial behavior. *Mechanics of Materials*, 79, 45–57.
- Pourghahramani, P., & Forssberg, E. (2005). Review of applied particle shape descriptors and produced particle shapes in grinding environments. Part I: Particle shape descriptors. *Mineral Processing and Extractive Metallurgy Review*, 26(2), 145–166.
- Remond, S., & Pizette, P. (2014). A DEM hard-core soft-shell model for the simulation of concrete flow. *Cement and Concrete Research*, 58, 169–178.
- Rocco, C. G., & Elices, M. (2009). Effect of aggregate shape on the mechanical properties of a simple concrete. *Engineering Fracture Mechanics*, 76(2), 286–298.
- Sarfarazi, V., Ghazvinian, A., Schubert, W., Blumel, M., & Nejati, H. R. (2014). Numerical simulation of the process of fracture of echelon rock joints. *Rock Mechanics and Rock Engineering*, 47(4), 1355–1371.
- Sarfarazi, V., & Haeri, H. (2016). A review of experimental and numerical investigations about crack propagation. *Computers and Concrete*, 18(2), 235–266.
- Sarfarazi, V., & Schubert, W. (2017). Numerical simulation of tensile failure of concrete in direct, flexural, double punch tensile and ring tests. *Periodica Polytechnica: Civil Engineering*, 61(2), 176–183.
- Schultz, R. A. (1993). Brittle strength of basaltic rock masses with applications to venus. *Journal of Geophysical Research: Planets*, 98(E6), 10883–10895.

- Schultz, R. A. (1995). Limits on strength and deformation properties of jointed basaltic rock masses. *Rock Mechanics and Rock Engineering*, 28(1), 1–15.
- Shigang, A., Liquan, T., Yiqi, M., Yongmao, P., Yiping, Liu, & Daining, Fang. (2013). Effect of aggregate distribution and shape on failure behavior of polyurethane polymer concrete under tension. *Computational Materials Science*, 67, 133–139.
- Shuguang, L., & Qingbin, L. (2015). Method of meshing ITZ structure in 3D meso-level finite element analysis for concrete. *Finite Elements in Analysis and Design*, 93, 96–106.
- Shyshko, S., & Mechtcherine, V. (2013). Developing a discrete element model for simulating fresh concrete: Experimental investigation and modelling of interactions between discrete aggregate particles with fine mortar between them. *Construction and Building Materials*, 47, 601–615.
- Simeonov, P., & Ahmad, S. (1995). Effect of transition zone on the elastic behavior of cement-based composites. *Cement and Concrete Research*, 25(1), 165–176.
- Tan, Y., Deng, R., Feng, Y. T., Zhang, H., & Jiang, S. (2015). Numerical study of concrete mixing transport process and mixing mechanism of truck mixer. *Engineering Computations*, 32(4), 1041–1065.
- Wang, Z., Lin, F., & Xianglin, G. (2008). Numerical simulation of failure process of concrete under compression based on mesoscopic discrete element model. *Tsinghua Science & Technology*, 13(Supplement 1), 19–25.
- Wu, F. 2006. Experimental study on whole stress–strain curves of concrete under axial tension. Master's thesis, Hunan University. **(in Chinese)**.
- Xianglin, G., Hong, L., Wang, Z., & Lin, F. (2013). Experimental study and application of mechanical properties for the interface between cobblestone aggregate and mortar in concrete. *Construction and Building Materials*, 46, 156–166.
- Yang, C. C. (1998). Effect of the transition zone on the elastic moduli of mortar. *Cement and Concrete Research*, 28(5), 727–736.
- Yiqiang, L. I., Xinmin, W., & Shitong, C. (2005). Comparison of stress–strain curves for concrete under uniaxial stresses. *Journal of Highway and Transportation Research and Development*, 22(10), 75–78. (in Chinese).
- You, T., Abu Al-Rub, R., Masad, E., & Little, D. (2012). Three-dimensional microstructural modeling of asphalt concrete using a unified viscoelastic–viscoplastic–viscodamage model. *Construction and Building Materials*, 28(1), 531–548.
- Zhang, S., Wang, G., Wang, C., Pang, B., & Chengbo, Du. (2014). Numerical simulation of failure modes of concrete gravity dams subjected to underwater explosion. *Engineering Failure Analysis*, 36, 49–64.
- Zhenhai G. 1997. *Strength and deformation of concrete: experimental basis and constitutive relation*, volume 4. Tsinghua University Press. **(in Chinese)**.

Submit your manuscript to a SpringerOpen[®] journal and benefit from:

- Convenient online submission
- Rigorous peer review
- Open access: articles freely available online
- High visibility within the field
- Retaining the copyright to your article

Submit your next manuscript at ► springeropen.com
